

Efficient Lithium Metal Cycling over a Wide Range of Pressures from an Anion-Derived Solid-Electrolyte Interphase Framework

Hansen Wang, William Huang, Zhiao Yu, Wenxiao Huang, Rong Xu, Zewen Zhang, Zhenan Bao,* and Yi Cui*



Cite This: *ACS Energy Lett.* 2021, 6, 816–825



Read Online

ACCESS |



Metrics & More

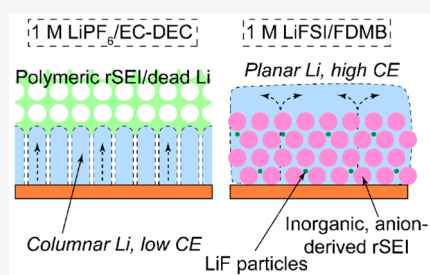


Article Recommendations



Supporting Information

ABSTRACT: Advanced electrolytes were developed to improve the cyclability of lithium (Li) metal anodes, yet their working mechanisms remain unclear. Here, we study the Li cycling performance under different pressures in a 1 M Li bis(fluorosulfonyl)imide/fluorinated 1,4-dimethoxybutane electrolyte. A consistently long cycle life is achieved over a wide range of pressures (30–600 psi). This is due to a completely different Li plating mode with more favorable deposition morphologies compared to that in a conventional carbonate electrolyte, which exhibits increasing cycle stability with increased pressure. We show that this is enabled by the properties of an anion-derived residual solid-electrolyte interphase (rSEI) framework on the electrode surface, an undercharacterized structure with profound implications for Li metal cycling. This anion-derived rSEI chemistry is likely the key to a prolonged cycle life of Li metal batteries and should be vigorously addressed in future electrolyte designs.



With a low electrode potential (−3.04 V) and a high specific capacity (3860 mAh/g), lithium (Li) metal anodes have great potential for the realization of next-generation batteries with high specific energies.^{1,2} However, commercialization of Li metal anodes is plagued by their poor cyclability, rooted in their high chemical reactivity, dendritic growth pattern, and large change in volume during Li metal deposition.³ A series of approaches, such as the design of “host” structures^{4–11} and artificial solid-electrolyte interphases (SEIs),^{12–16} have been utilized to address these issues.^{17–19} Still, the cycling performance of Li metal anodes is far from what would be required for practical applications. Recently, electrolyte engineering has arisen as one of the most promising strategies. A series of advanced electrolyte systems, including high-concentration electrolytes (HCEs),^{20–23} localized high-concentration electrolytes (LHCEs),^{24–28} dual-salt electrolytes,^{29–31} all-fluorinated electrolytes,^{32–34} liquefied gas electrolytes,^{35–37} and a single-salt, single-solvent electrolyte,³⁸ altered the deposition morphology of Li metal, leading to much improved Coulombic efficiencies (CEs). The improved CEs in these advanced electrolytes were usually attributed to a much more passivating compact SEI (cSEI, the SEI film in intimate contact with the Li metal surface).^{20,28,39–43} However, this theory cannot explain why the CEs of many advanced electrolytes are lower during initial cycles than those of baseline carbonate electrolytes (Figure S1), and then gradually increase during continuous cycling.

Furthermore, a recent study (unpublished results) shows that Li metal corrodes at similar or even faster rates in some of the advanced electrolytes than in baseline carbonate electrolytes during storage, suggesting that the compact SEIs in these advanced electrolytes are not as passivating as expected. Therefore, a thorough understanding of the working mechanisms of these high-performing electrolytes remains lacking.

Compared to that of Li-ion batteries, operation of Li metal batteries leads to more pronounced pressure fluctuation due to the aggravated electrode volume change.^{29,44} However, pressure is rarely regulated or optimized for the testing of Li metal batteries with advanced electrolytes. Experimental and simulation studies indicated that increased pressure was generally beneficial for Li cycling but also dependent on the electrolyte.^{45,46} Because the recently reported advanced electrolytes enabled Li deposition in favorable yet slightly varied morphologies,^{24,28,29,32} the dependencies of their performance on pressure are thus an interesting and critical

Received: December 5, 2020

Accepted: February 1, 2021

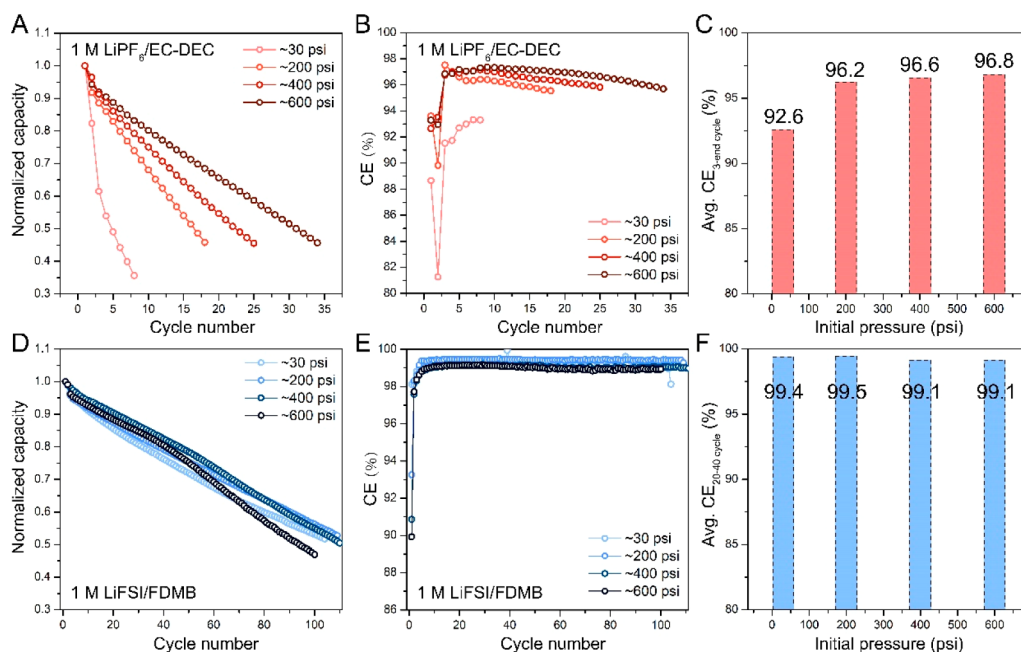


Figure 1. Cycling of anode-free pouch cells under various initial pressures using different electrolytes. (A) Evolution of normalized discharge capacity vs cycle number under different initial pressures in the 1 M LiPF₆/EC-DEC electrolyte. (B) Cycling CE under different initial pressures in the 1 M LiPF₆/EC-DEC electrolyte. (C) Average CE analysis under different initial pressures in the 1 M LiPF₆/EC-DEC electrolyte. (D) Evolution of the normalized discharge capacity vs cycle number under different initial pressures in the 1 M LiFSI/FDMB electrolyte. (E) Cycling CE under different initial pressures in the 1 M LiFSI/FDMB electrolyte. (F) Average CE analysis under different initial pressures in the 1 M LiFSI/FDMB electrolyte.

topic but have been rarely studied. Such a study will also provide valuable insights about the Li deposition mechanisms. Pressure in commonly used coin cell testing is hard to regulate due to the varying electrode thicknesses and the number of spacers used. The springs may also lead to non-uniform pressure within a single coin cell. Therefore, a systematic study of Li metal pouch cell cycling performance against pressure within various electrolyte systems is desired.

In this paper, a baseline 1 M LiPF₆/ethylene carbonate (EC)-diethyl carbonate (DEC) [1:1 (v:v)] system and a high-performance 1 M Li bis(fluorosulfonyl)imide (LiFSI)/fluorinated 1,4-dimethoxybutane (FDMB)³⁸ system are chosen as model electrolyte systems to characterize Li metal cycling performance against pressure using anode-free pouch cells. Cells in the two different electrolytes show divergent cycle life dependencies on pressure, suggestive of different Li plating modes. Such different Li plating modes are subsequently elucidated and cross-validated using scanning electron microscopy (SEM), pressure analysis, and electrochemical methods. In the 1 M LiPF₆/EC-DEC electrolyte, Li metal deposits in filamentary shapes beneath accumulated residual SEI (rSEI), which is the SEI remaining on the electrode surface after Li metal stripping. In the 1 M LiFSI/FDMB electrolyte, on the contrary, Li penetrates the porous rSEI to form a homogeneous, planar structure above it. The different Li plating patterns are further correlated to the distinct rSEI chemistries, which were characterized through SEM energy-dispersive X-ray spectroscopy (EDS) and cryogenic scanning transmission electron microscopy (cryo-STEM) electron energy loss spectroscopy (EELS). The rSEI in the 1 M LiPF₆/EC-DEC electrolyte is dominated by organic species, while that in the 1 M LiFSI/FDMB electrolyte is mainly anion-derived with LiF nanoparticles dispersed within its framework. Finally, experiments are performed to prove that

the formation of rSEI is critical to the high Li CE in the 1 M LiFSI/FDMB electrolyte. We believe this unique anion-derived inorganic rSEI framework is likely the key to achieving an improved Li deposition morphology, as well as a prolonged cycle life.

Li metal cycling performance against pressure is first characterized utilizing anode-free pouch cells with a total capacity of ~120 mAh (Figure S2a). Li iron phosphate (LFP) is chosen as the cathode for two reasons. First, it possesses near 100% CE during the first cycle. Therefore, compared to CullLi nickel manganese cobalt oxide (NMC) cells that have a low first-cycle CE so that a Li reservoir could form to compensate for subsequent capacity loss, CullLFP cells show faster capacity decay. However, this is beneficial for this study because the CullLFP full cell CE thus represents the Li metal cycling CE and can be directly correlated to the Li plating patterns. Second, with the low operation voltage of LFP, Li loss due to electrolyte decomposition on the cathode side is minimized. As a result, capacity decay can be attributed solely to the corrosion of Li during its deposition and stripping on the anode side. The pouch cells are cycled with fixed thicknesses, and their pressure fluctuations are monitored through a pressure sensing system *in operando* (Figure S2b). The 1 M LiPF₆/EC-DEC and 1 M LiFSI/FDMB systems are used as model electrolytes for comparison. For each electrolyte, the initial cycling pressure is set as 30, 200, 400, and 600 psi.

The cycling results are shown in Figure 1. Cells with the 1 M LiFSI/FDMB electrolyte present significantly higher capacity retention and CE compared to cells with the 1 M LiPF₆/EC-DEC electrolyte even under low initial pressures that were considered to result in inferior performances. Meanwhile, the performance against pressure using the two electrolytes also shows different trends. For the 1 M LiPF₆/EC-DEC system, capacity retention and CE both grow continuously with

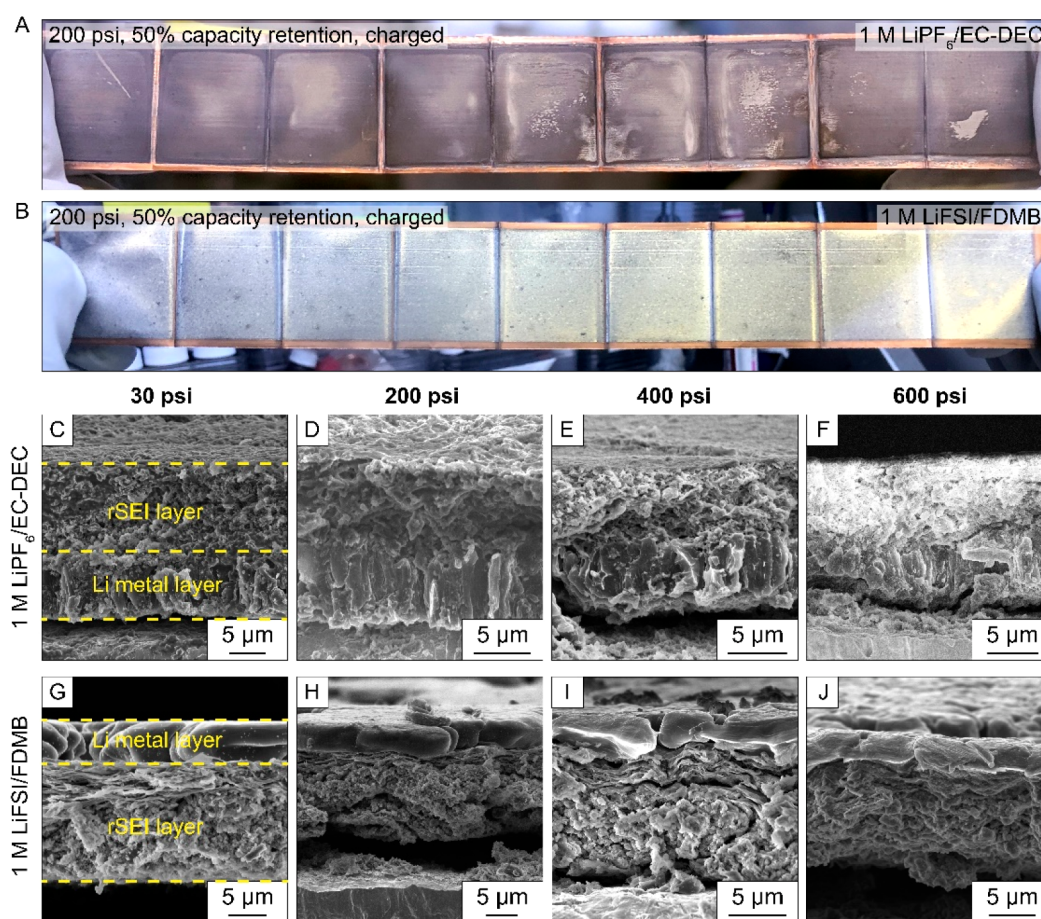


Figure 2. Morphology of deposited Li metal after 50% capacity decay using different electrolytes. (A and B) Digital photos of the Cu surfaces under charged states with the 1 M LiPF₆/EC-DEC and 1 M LiFSI/FDMB electrolytes, respectively. (C–F) SEM images of the cross sections of Li metal deposits using the 1 M LiPF₆/EC-DEC electrolyte with initial pressures of 30, 200, 400, and 600 psi, respectively. Li metal deposits in a columnar morphology beneath the rSEI layer under all pressures. (G–J) SEM images of the cross sections of Li metal deposits using the 1 M LiFSI/FDMB electrolyte with initial pressure of 30, 200, 400, and 600 psi, respectively. Li metal deposits through the rSEI layer to the top surface in a planar morphology under all pressures.

increasing cycling pressure (Figure 1A–C). In contrast, for the 1 M LiFSI/FDMB system, the capacity retention and CE have a very weak response to pressure. Even under a low initial pressure of ~30 psi, the cell still shows a high CE and a long cycle life. Even more surprisingly, small decays in the CE can be observed under extremely high pressures (~400–600 psi), possibly due to the enhanced edge effects. The different dependencies of performance on initial pressure suggest intrinsically distinct Li metal deposition patterns in the different electrolyte systems, which we characterize in the next section.

The pouch cells tested are disassembled in the fully charged states after the discharge capacity decays to 50% of the initial capacity. Significant differences can be observed optically on the anode (Cu foil) surfaces (Figure 2). For pouch cells using the 1 M LiPF₆/EC-DEC electrolyte, the anodes show dark color under all initial pressures (Figure 2A and Figure S3), indicating the absence of metallic Li on the top surfaces. For cells with the 1 M LiFSI/FDMB electrolyte, the anodes appear to be silver under all pressures (Figure 2B and Figure S4), indicating the existence of metallic Li with a homogeneous morphology at the top surfaces.

SEM is then used to observe the cross sections of these cycled anodes, and the results further verify the optical inspection above. SEI shells usually cannot be reused during Li

metal cycling;⁴³ thus, the discarded SEI shells will accumulate and form a layer of the rSEI framework on the Cu surface after continuous cycling. Under SEM, Li metal is observed to deposit beneath the rSEI into a columnar morphology in the 1 M LiPF₆/EC-DEC electrolyte under various pressures (Figure 2C–F). In contrast, Li metal grows on top of the rSEI into a planar morphology in the 1 M LiFSI/FDMB electrolyte (Figure 2G–J). Due to the poor electron conductivity of SEI, Li metal must still nucleate on the Cu foil but then likely penetrates through the rSEI layer to reach the outer surface, which is directly observed from an anode from a cell disassembled with a higher capacity retention (Figure S5). Further discussion of the different Li plating modes through pressure analysis and electrochemical methods is provided in Supplementary Notes. Plan view SEM is performed, as well. In the 1 M LiPF₆/EC-DEC electrolyte, the rSEI layer on the top surface appears to be more porous (30 psi). The existence of dead Li can also be observed under an initial pressure of 30 psi (Figure S6). This suggests that the consistent increase in cycling performance with pressure in this electrolyte can be mainly attributed to the enhanced mechanical force applied. Disconnected or “dead” Li is the principal means of capacity loss in Li metal batteries, especially within baseline carbonate electrolytes;⁴⁷ under increased pressure, Li metal along with the rSEI is compacted into denser structures, leading to

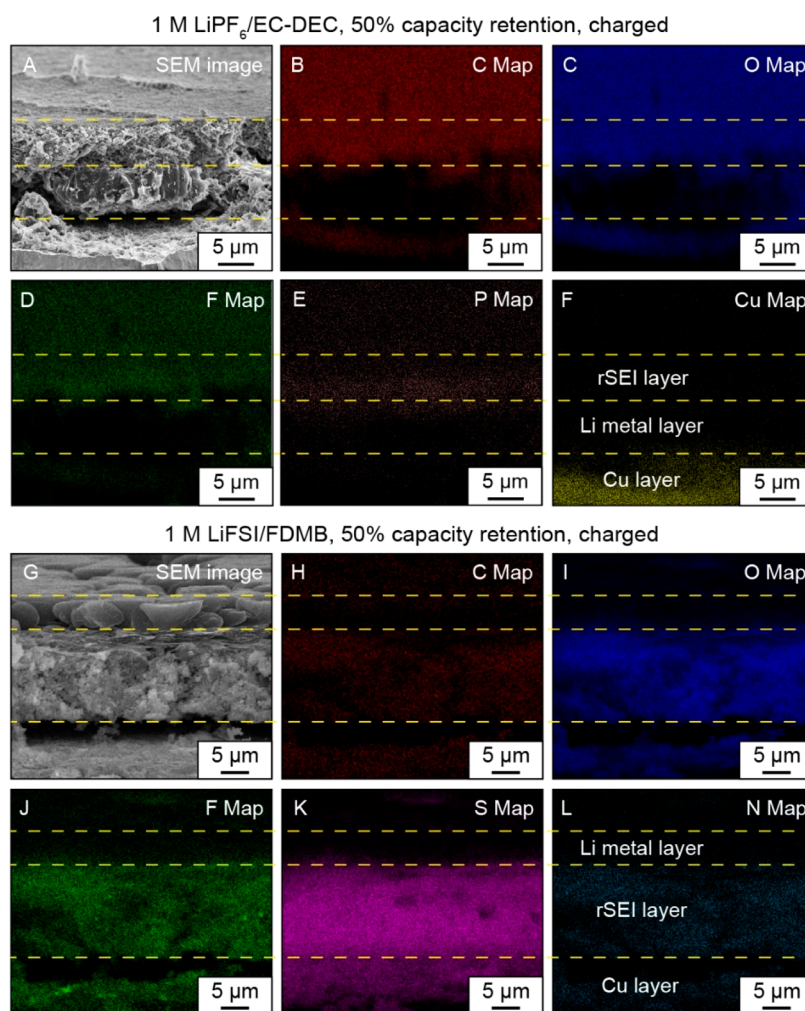


Figure 3. SEM-EDS characterizations of the rSEI. (A–F) SEM-EDS mapping for the elemental distributions on the cross section of a charged anode cycled to 50% capacity retention in the 1 M LiPF₆/EC-DEC electrolyte. (G–L) SEM-EDS mapping for the elemental distributions on the cross section of a charged anode cycled to 50% capacity retention in the 1 M LiFSI/FDMB electrolyte.

minimized dead Li during stripping and improved CE. However, in the 1 M LiFSI/FDMB electrolyte, the Li metal deposited on the outer surface shows a consistently planar morphology with a small surface area (Figure S7), accounting for its outstanding performance even under a low initial pressure of 30 psi. The fact that Li metal can deposit uniformly even under low pressures along with the unique plating morphology in the 1 M LiFSI/FDMB electrolyte suggests that the chemical properties of the rSEI may play a critical role in the performance, which we subsequently characterize.

SEM-EDS (Figure 3) is first used to characterize the elemental distribution on the cross sections of the samples shown in panels E and I of Figure 2. The top rSEI layer in the 1 M LiPF₆/EC-DEC electrolyte contains strong C, O, F, and P signals, while the top Li metal layer in the 1 M LiFSI/FDMB electrolyte shows weak overall X-ray signals (Li cannot be detected in windowed EDS detectors). This is consistent with the different plating patterns of Li metal discussed previously. The rSEI layer in the 1 M LiPF₆/EC-DEC electrolyte is enriched with C and O (Figure 3B,C and Figure S8a), indicating the polymeric nature of the rSEI framework, likely originating from the decomposition products of the EC solvent.⁴⁸ In contrast, both the SEM-EDS spectra (Figure S8b) and elemental mapping (Figure 3H) present a much

weaker C signal in the 1 M LiFSI/FDMB electrolyte, indicating that the rSEI is dominated by inorganic species. Furthermore, O, F, S, and N (main elements in the FSI⁻ anion) are distributed in very similar patterns (Figure 3I–L), indicating the rSEI chemistry resembles that of the FSI⁻ anion and is likely composed of its reduction products, in good agreement with previous X-ray photoelectron spectroscopy (XPS) and cryo-TEM EDS analysis of the SEI in this electrolyte.³⁸ This anion-derived feature suggests that the rSEI is a good Li⁺ conductor, which may serve to homogenize the Li⁺ flux at the electrode/rSEI interface and aid in the deposition of flat, nondendritic Li metal.

Atomic force microscopy (AFM) nanoindentation is further performed to characterize the elastic modulus of the rSEI formed in the two electrolytes (Figure S9). Pouch cells are cycled under an initial pressure of 200 psi to 50% capacity retention and disassembled in the discharged states. Afterward, the distributions and histograms of the elastic modulus of the rSEI are analyzed. For the 1 M LiPF₆/EC-DEC electrolyte, the average rSEI elastic modulus is 0.48 ± 0.11 GPa (Figure S9c), resembling that of the organic SEI species reported in other works.^{49,50} In contrast, the average elastic modulus is 3.5 ± 1.2 GPa for the rSEI formed in the 1 M LiFSI/FDMB electrolyte (Figure S9f) with an elastic modulus of 15–20 GPa distributed

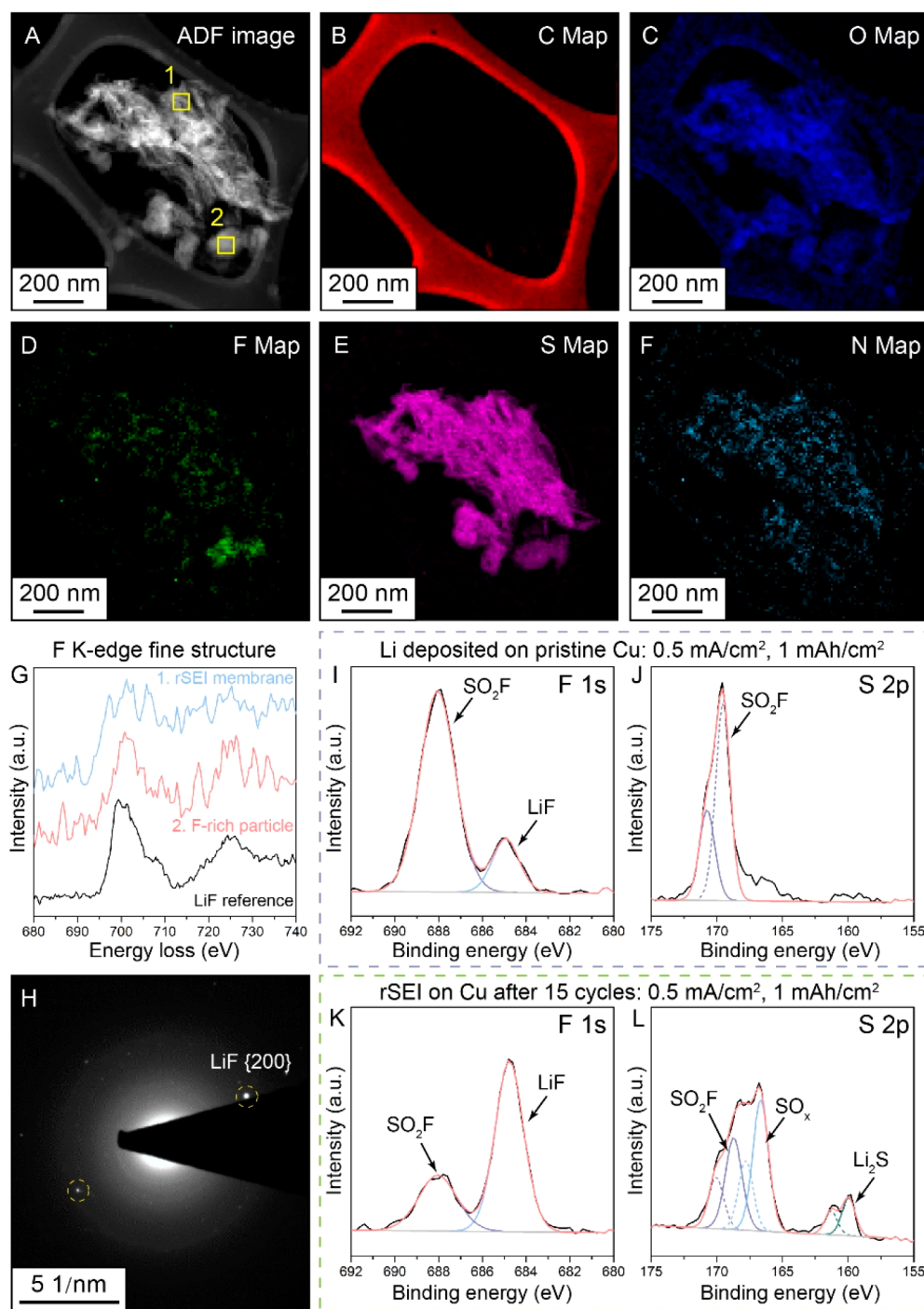


Figure 4. Cryo-STEM EELS, SAED, and XPS characterizations of the rSEI. (A–F) Cryo-STEM EELS mapping of a rSEI particle scratched from the surface of a Cu electrode after 15 cycles under 0.5 mA/cm² and 1 mAh/cm² in the 1 M LiFSI/FDDB electrolyte. (G) F K-edge fine structure compared between the two yellow boxes in panel A. (H) SAED pattern of the rSEI showing the existence of crystalline LiF. (I and J) XPS F 1s and S 2p spectra, respectively, of a Li surface deposited onto a Cu foil under 0.5 mA/cm² and 1 mAh/cm². (K and L) XPS F 1s and S 2p spectra, respectively, of the rSEI left on a Cu foil after 15 cycles under 0.5 mA/cm² and 1 mAh/cm². The electrolyte used for this figure is 1 M LiFSI/FDDB.

in some of the detected spots, which is an order of magnitude higher than the rSEI in the 1 M LiPF₆/EC-DEC electrolyte and resembles that of inorganic SEI species.⁴⁹ Small deviations from previous works might arise from the different mesoscale structure, such as the rSEI framework porosity and molecular arrangement.⁵¹ Overall, the elastic modulus data are highly consistent with the different rSEI chemical compositions elucidated from the SEM-EDS results presented above.

To further study the inorganic rSEI species in the 1 M LiFSI/FDDB electrolyte, cryo-STEM EELS is used for high-spatial and -spectral resolution characterizations. The sample we used is the rSEI scratched from a Cu electrode cycled in the 1 M LiFSI/FDDB electrolyte (Figure 4A). The C signal in the rSEI is weak (Figure 4B), with the C signal primarily originating from the carbonaceous support film of the TEM grid, confirming its inorganic nature. Elemental distributions of

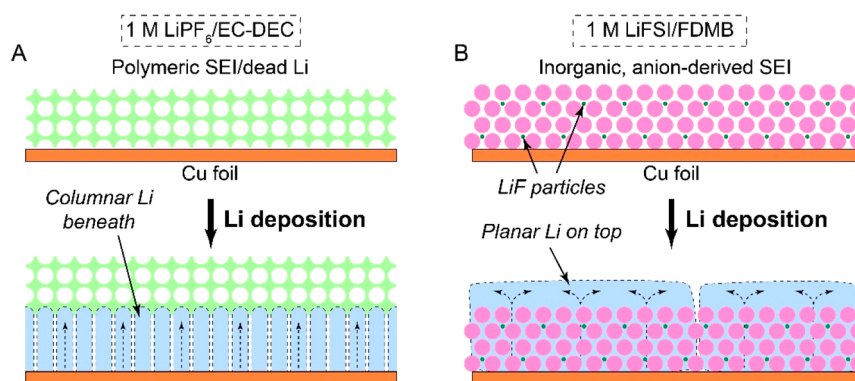


Figure 5. Schematic of the different Li plating modes in 1 M LiPF₆/EC-DEC and 1 M LiFSI/FDMB electrolytes. (A) In the 1 M LiPF₆/EC-DEC electrolyte, rSEI is composed of a polymeric framework. During deposition, Li metal grows beneath the rSEI into a columnar morphology. (B) In the 1 M LiFSI/FDMB electrolyte, rSEI is mainly anion-derived but with scattered LiF nanoparticles. During deposition, Li metal grows through the rSEI into a planar morphology on the top surface.

O, F, S, and N are again similar (Figure 4C–F), indicating an anion-derived chemistry. Some locations within the sample (box 2 in Figure 4A) are found to be further enriched with F while weak in O, S, and N. The F K-edge EELS fine structure is thus studied for comparison (Figure 4G). The F K-edge fine structure in this region resembles that of F in the LiF reference to a great extent, while the F fine structure elsewhere (box 1 in Figure 4A as an example) is very much different, indicative of the different F bonding environments within the rSEI. Selected area electron diffraction (SAED) of the rSEI sample further confirms the existence of crystalline LiF (Figure 4H). These findings show the existence of two F moieties within the rSEI: FSI[−] analogue species as well as LiF nanoparticles embedded within the rSEI framework.

To further study this phenomenon, XPS results are studied. The elemental ratio is first compared between the rSEIs in the 1 M LiPF₆/EC-DEC and 1 M LiFSI/FDMB electrolytes (Tables S1 and S2). The C ratio is significantly lower within the rSEI of the 1 M LiFSI/FDMB electrolyte, consistent with the EELS results presented above. rSEI in the 1 M LiFSI/FDMB electrolyte also shows an increased ratio of F, N, and S. Afterward, XPS fine structures are compared between two different samples cycled in the 1 M LiFSI/FDMB electrolyte. Sample 1 is 1 mAh/cm² of Li metal deposited onto a pristine Cu foil under 0.5 mA/cm² (Figure 4I,J), and sample 2 is the rSEI left on a Cu electrode after 15 cycles under 0.5 mA/cm² and 1 mAh/cm² (Figure 4K,L). Both -SO₂F (FSI[−] analogue species) and LiF can be observed in the F 1s fine structures of both samples. For sample 1, the LiF signal is much weaker than the -SO₂F signal in the F 1s peak, and the S 2p peak is dominated by -SO₂F. In contrast, for sample 2, the LiF signal grows much stronger in the F 1s peak, and new sulfur species such as -SO_x and Li₂S appeared in the S 2p peak. The stronger LiF and Li₂S signals in sample 2 are further validated by the Li 1s peak results (Figure S10). These results indicate that there is a trend of -SO₂F decomposing (possibly with the participation of Li metal) into Li₂S, -SO_x, and the LiF nanoparticles observed in previous characterizations.

From our morphological and chemical characterizations of Li metal plating in different electrolytes, it becomes possible to propose pathways in which the rSEI properties influence the final Li metal microstructure (Figure 5). In the 1 M LiPF₆/EC-DEC electrolyte (Figure 5A), rSEI is composed of significant amounts of polymeric species that agglomerate to conformally cover the Li metal surface. As a result, Li metal tends to deposit

beneath the rSEI framework into columnar structures. Increased pressure promotes denser Li deposition, leading to a decreased level of dead Li formation and improved CE. In contrast, in the 1 M LiFSI/FDMB electrolyte (Figure 5B), the rSEI is dominated by inorganic, anion-derived species, with LiF nanoparticles dispersed within its framework. During Li deposition, Li grows through the porous rSEI framework into a planar morphology on the top surface, even under a low operational pressure of ~30 psi. The unique rSEI chemistry in the 1 M LiFSI/FDMB electrolyte appears to be the reason for the high CE of Li metal. Additionally, the construction of the rSEI framework through accumulation of electrolyte decomposition products is likely the key reason for the gradual CE increase during the initial cycles of this electrolyte (Figure S1).

To further correlate the formation of the rSEI framework to a high Li cycling performance in the 1 M LiFSI/FDMB electrolyte, we compare the CE and morphology of Li deposited onto a pristine Cu surface to those on an “activated” Cu surface already covered with rSEI (Figure 6). For the CE comparison, a coin cell experiment is performed. Pristine Cu electrodes (with no pretreatment or washing) are first paired with Li metal in half-cells and subsequently cycled to build an rSEI layer on the Cu. The coin cells are disassembled after 15 cycles (with Li fully stripped away from the Cu electrode), and the cycled Cu electrodes (activated Cu) are rinsed with FDMB solvent and dried subsequently. Activated Cu electrodes are paired with new Li counter electrodes in a fresh 1 M LiFSI/FDMB electrolyte for half-cell cycling again. The Li cycling CE can be then compared between pristine Cu and activated Cu. It can be observed that first-cycle CEs using pristine Cu remain only around ~90%, while those using activated Cu increased to nearly 98% (Figure 6A,B). The average CE in the first 10 cycles also shows significant improvement after the Cu surface is activated. This confirms that the source of the CE increase in the early cycles of Li metal in the 1 M LiFSI/FDMB electrolyte is the construction of an rSEI framework on the Cu surface, rather than any changes in electrolyte chemistry.

Further evidence is provided through SEM characterization of the Li deposited during the first and second cycles (Figure 6C–F). The samples are retrieved from anode-free pouch cells cycled under an initial pressure of ~200 psi. Li deposits into ~3 μm granules with larger surface areas during the first cycle (Figure 6C). A considerable amount of small Li spheres (~1 μm diameter) also disperses on the direct surface of Cu foil, which will further undermine the cycling CE with their high

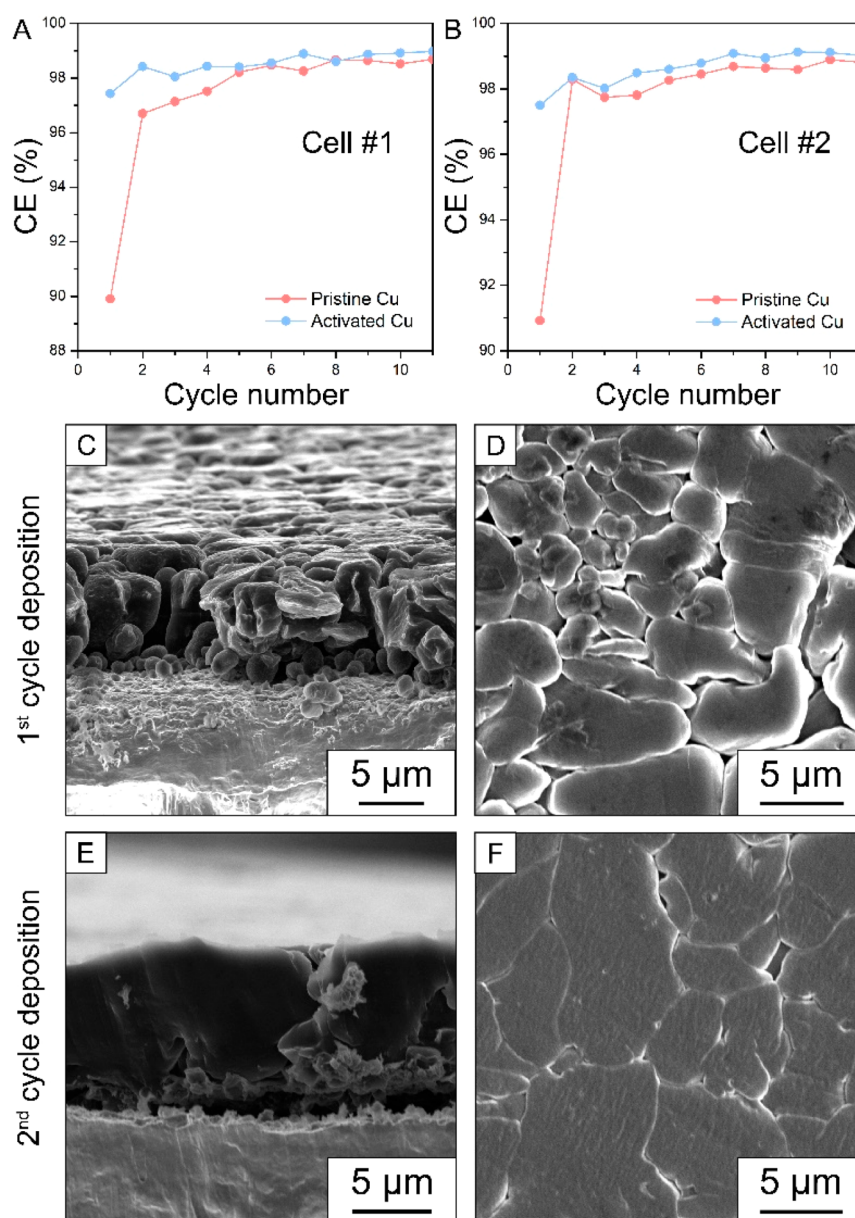


Figure 6. Comparison of Li deposition on pristine and cycled Cu surfaces in the 1 M LiFSI/FDMB electrolyte. (A and B) CullLi coin cell cycling CE comparison between pristine Cu and activated Cu. (C and D) SEM images of the cross section and top view, respectively, of Li deposited on Cu foil during the first cycle. The sample is prepared from an anode-free pouch cell cycled under an initial pressure of 200 psi. (E and F) SEM images of the cross section and top view, respectively, of Li deposited on Cu foil during the second cycle. The sample is prepared from an anode-free pouch cell cycled under an initial pressure of 200 psi.

surface area:volume ratio. Plan view SEM also shows a high porosity that possibly enables the electrolyte to immerse and corrode the deposited Li (Figure 6D). In contrast, Li deposited during the second cycle (on the Cu already covered with the rSEI from the first cycle) shows a significantly increased particle size over 10 μm with barely any porosity (Figure 6E). The dense and homogeneous morphology observed from the top view resembles that of the samples at 50% capacity retention shown previously. As the cell pressure remains similar at the beginning of the first and second cycles, the boost in the efficiency originates from the chemical activation of the Cu surface, that is, the formation of the rSEI layer. The low initial CE in inactivated Cu cells arises from the more porous, large-surface area Li plating morphology in the initial cycles, before a stabilizing rSEI framework is constructed.

Finally, we propose some possible mechanisms of how the rSEI framework in the 1 M LiFSI/FDMB electrolyte promotes Li deposition morphology and CE. First, multiple designs of artificial SEI have been introduced to enable high Li cycling performance.^{14,15,52–54} It has been reported that some of these artificial SEI layers can modulate the SEI/Li interfacial energy to promote better Li deposition morphologies.^{52,53} The special rSEI formed in the 1 M LiFSI/FDMB electrolyte might serve a similar role. With a potentially lower rSEI/Li interfacial energy, Li metal would preferentially spread out on the surfaces of rSEI forming large grains. Second, it has been reported that LiF particles can lower the diffusion energy barrier at the Li/electrolyte interface, promoting planar rather than dendritic Li deposition.^{6,55–57} The planar Li deposition is exactly what we observe in the 1 M LiFSI/FDMB electrolyte, where the

accumulation of LiF nanoparticles in the rSEI framework is also confirmed. However, we do believe that the FSI⁻ analogue chemicals are also critical. This is because LiFSI seems to be unique in improving the Li cycling performance in various reported electrolyte recipes.^{20–24,26,28,38} Higher anion ratios in the solvation structures have also been reported for most of these high-performing electrolytes.^{20,28} LiF, in contrast, has also been observed in both the cSEI⁵⁸ and indirect SEI⁵⁹ formed in baseline carbonate electrolytes with inferior performances. It is highly likely that a synergetic effect exists between the F- and S-rich anion-derived species that enhances Li⁺ conductivity and homogenizes Li⁺ flux and LiF nanoparticles that modulates the interfacial energy and surface Li diffusivity to further promote uniform Li deposition. Nevertheless, elucidation of the exact mechanism calls for further investigations of the rSEI properties in the future.

In summary, operational pressure is optimized for different electrolytes using multilayer anode-free pouch cells. Li cycling performance in the 1 M LiPF₆/EC-DEC electrolyte monotonically improves with an increased initial pressure, while that in the 1 M LiFSI/FDDB electrolyte is weakly dependent on initial pressure. This is attributed to the entirely different Li plating modes on the rSEI-covered Cu surface between the two electrolytes. In the conventional 1 M LiPF₆/EC-DEC electrolyte, the rSEI is composed of a polymeric framework, blocking Li metal penetration so that it can only deposit beneath. An increased operational pressure promotes a more homogeneous Li deposition morphology with better CE through the mechanical compaction of the Li metal layer. In the 1 M LiFSI/FDDB electrolyte, rSEI is dominated by anion-derived species with accumulated LiF nanoparticles. Li grows through the rSEI layer into a planar morphology on the outer surface. We further prove that the consistently dense Li deposition pattern even under a low initial pressure (30 psi) is enabled by the unique chemical properties of the rSEI. This anion-derived rSEI is likely the key to promoting the Li cycling efficiency reported in the 1 M LiFSI/FDDB electrolyte, as well as various Li compatible electrolytes using LiFSI.

Deposition morphology has been known to have a significant impact on the Li cycling CE.⁴⁷ Our work indicates that the structure and chemistry of the rSEI, which have rarely been addressed in previous works, are possibly much more critical to an improved Li deposition pattern and the subsequent high CE than that of the cSEI (further discussions in [Supplementary Notes](#)). We believe that further identifications of the FSI⁻-derived rSEI species and comparison experiments between various anion chemistries will be crucial for thoroughly elucidating the origin of improved Li cycling performances within these electrolyte systems. This will be of great value in guiding future electrolyte engineering to enable practical high-specific energy Li metal batteries.

■ ASSOCIATED CONTENT

SI Supporting Information

The Supporting Information is available free of charge at <https://pubs.acs.org/doi/10.1021/acsenergylett.0c02533>.

Detailed experimental methods; supplementary notes and analyses; and supplementary battery data, optical images, and SEM, AFM, XPS, and pressure evolution data (PDF)

■ AUTHOR INFORMATION

Corresponding Authors

Zhenan Bao – Department of Chemical Engineering, Stanford University, Stanford, California 94305, United States; orcid.org/0000-0002-0972-1715; Email: zbao@stanford.edu

Yi Cui – Department of Materials Science and Engineering, Stanford University, Stanford, California 94305, United States; Stanford Institute for Materials and Energy Sciences, SLAC National Accelerator Laboratory, Menlo Park, California 94305, United States; orcid.org/0000-0002-6103-6352; Email: yicui@stanford.edu

Authors

Hansen Wang – Department of Materials Science and Engineering, Stanford University, Stanford, California 94305, United States; orcid.org/0000-0002-6738-1659

William Huang – Department of Materials Science and Engineering, Stanford University, Stanford, California 94305, United States; orcid.org/0000-0001-8717-5337

Zhiao Yu – Department of Chemical Engineering and Department of Chemistry, Stanford University, Stanford, California 94305, United States; orcid.org/0000-0001-8746-1640

Wenxiao Huang – Department of Materials Science and Engineering, Stanford University, Stanford, California 94305, United States

Rong Xu – Department of Materials Science and Engineering, Stanford University, Stanford, California 94305, United States

Zewen Zhang – Department of Materials Science and Engineering, Stanford University, Stanford, California 94305, United States; orcid.org/0000-0002-4909-4330

Complete contact information is available at:

<https://pubs.acs.org/10.1021/acsenergylett.0c02533>

Author Contributions

H.W., W.H., and Z.Y. contributed equally to this work. H.W., W.H., Z.Y., Z.B., and Y.C. conceived the project and designed the experiments. H.W. carried out battery fabrication and testing. W.H. performed SEM and STEM. Z.Y. synthesized electrolytes. W.H. helped with pressure monitoring and analysis. R.X. performed AFM. Z.Z. helped with SEM. H.W., W.H., Z.Y., Z.B., and Y.C. co-wrote the manuscript, with input from all authors.

Notes

The authors declare the following competing financial interest(s): The 1 M LiFSI/FDDB electrolyte used in this work has been filed as U.S. Provisional Patent Application 62/928,638.

■ ACKNOWLEDGMENTS

This work is supported by the U.S. Department of Energy, under the Assistant Secretary for Energy Efficiency and Renewable Energy, Office of Vehicle Technologies, the Battery Materials Research (BMR) Program, and Battery 500 Consortium. Part of this work was performed at the Stanford Nano Shared Facilities (SNSF), supported by the National Science Foundation under Grant ECCS-1542152.

REFERENCES

- (1) Lin, D.; Liu, Y.; Cui, Y. Reviving the lithium metal anode for high-energy batteries. *Nat. Nanotechnol.* **2017**, *12*, 194–206.
- (2) Chu, S.; Cui, Y.; Liu, N. The path towards sustainable energy. *Nat. Mater.* **2017**, *16*, 16–22.
- (3) Liu, B.; Zhang, J.-G.; Xu, W. Advancing Lithium Metal Batteries. *Joule* **2018**, *2*, 833–845.
- (4) Lin, D.; et al. Layered reduced graphene oxide with nanoscale interlayer gaps as a stable host for lithium metal anodes. *Nat. Nanotechnol.* **2016**, *11*, 626–632.
- (5) Yan, K.; et al. Selective deposition and stable encapsulation of lithium through heterogeneous seeded growth. *Nat. Energy* **2016**, *1*, 16010.
- (6) Wang, H.; Lin, D.; Liu, Y.; Li, Y.; Cui, Y. Ultrahigh-current density anodes with interconnected Li metal reservoir through overlithiation of mesoporous AlF_3 framework. *Science Advances* **2017**, *3*, No. e1701301.
- (7) Wang, H.; et al. Wrinkled Graphene Cages as Hosts for High-Capacity Li Metal Anodes Shown by Cryogenic Electron Microscopy. *Nano Lett.* **2019**, *19*, 1326–1335.
- (8) Wang, H.; et al. An Interconnected Channel-Like Framework as Host for Lithium Metal Composite Anodes. *Adv. Energy Mater.* **2019**, *9*, 1802720.
- (9) Liang, Z.; et al. Composite lithium electrode with mesoscale skeleton via simple mechanical deformation. *Sci. Adv.* **2019**, *5*, No. eaau5655.
- (10) Wang, H.; et al. Improving Lithium Metal Composite Anodes with Seeding and Pillaring Effects of Silicon Nanoparticles. *ACS Nano* **2020**, *14*, 4601–4608.
- (11) Chen, H.; et al. Tortuosity Effects in Lithium-Metal Host Anodes. *Joule* **2020**, *4*, 938–952.
- (12) Zheng, G.; et al. Interconnected hollow carbon nanospheres for stable lithium metal anodes. *Nat. Nanotechnol.* **2014**, *9*, 618–623.
- (13) Chen, H.; et al. Uniform High Ionic Conducting Lithium Sulfide Protection Layer for Stable Lithium Metal Anode. *Adv. Energy Mater.* **2019**, *9*, 1900858.
- (14) Yu, Z.; et al. A Dynamic, Electrolyte-Blocking, and Single-Ion-Conductive Network for Stable Lithium-Metal Anodes. *Joule* **2019**, *3*, 2761–2776.
- (15) Weng, Y.-T.; et al. An ultrathin ionomer interphase for high efficiency lithium anode in carbonate based electrolyte. *Nat. Commun.* **2019**, *10*, 5824.
- (16) Cheng, X.-B.; et al. A Review of Solid Electrolyte Interphases on Lithium Metal Anode. *Adv. Sci.* **2016**, *3*, 1500213.
- (17) Wang, H.; Liu, Y.; Li, Y.; Cui, Y. Lithium Metal Anode Materials Design: Interphase and Host. *Electrochem. Energy Rev.* **2019**, *2*, 509–517.
- (18) Cheng, X.-B.; Zhang, R.; Zhao, C.-Z.; Zhang, Q. Toward Safe Lithium Metal Anode in Rechargeable Batteries: A Review. *Chem. Rev.* **2017**, *117*, 10403–10473.
- (19) Liu, Y.; Zhou, G.; Liu, K.; Cui, Y. Design of Complex Nanomaterials for Energy Storage: Past Success and Future Opportunity. *Acc. Chem. Res.* **2017**, *50*, 2895–2905.
- (20) Qian, J.; et al. High rate and stable cycling of lithium metal anode. *Nat. Commun.* **2015**, *6*, 6362.
- (21) Fan, X.; et al. Highly Fluorinated Interphases Enable High-Voltage Li-Metal Batteries. *Chem.* **2018**, *4*, 174–185.
- (22) Ren, X.; et al. High-Concentration Ether Electrolytes for Stable High-Voltage Lithium Metal Batteries. *ACS Energy Lett.* **2019**, *4*, 896–902.
- (23) Suo, L.; et al. Fluorine-donating electrolytes enable highly reversible 5-V-class Li metal batteries. *Proc. Natl. Acad. Sci. U. S. A.* **2018**, *115*, 1156.
- (24) Ren, X.; et al. Enabling High-Voltage Lithium-Metal Batteries under Practical Conditions. *Joule* **2019**, *3*, 1662–1676.
- (25) Yu, L.; et al. A Localized High-Concentration Electrolyte with Optimized Solvents and Lithium Difluoro(oxalate)borate Additive for Stable Lithium Metal Batteries. *ACS Energy Lett.* **2018**, *3*, 2059–2067.
- (26) Chen, S.; et al. High-Efficiency Lithium Metal Batteries with Fire-Retardant Electrolytes. *Joule* **2018**, *2*, 1548–1558.
- (27) Chen, S.; et al. High-Voltage Lithium-Metal Batteries Enabled by Localized High-Concentration Electrolytes. *Adv. Mater.* **2018**, *30*, 1706102.
- (28) Cao, X.; et al. Monolithic solid-electrolyte interphases formed in fluorinated orthoformate-based electrolytes minimize Li depletion and pulverization. *Nat. Energy* **2019**, *4*, 796–805.
- (29) Weber, R.; et al. Long cycle life and dendrite-free lithium morphology in anode-free lithium pouch cells enabled by a dual-salt liquid electrolyte. *Nat. Energy* **2019**, *4*, 683–689.
- (30) Louli, A. J.; et al. Diagnosing and correcting anode-free cell failure via electrolyte and morphological analysis. *Nat. Energy* **2020**, *5*, 693–702.
- (31) Jiao, S.; et al. Stable cycling of high-voltage lithium metal batteries in ether electrolytes. *Nat. Energy* **2018**, *3*, 739–746.
- (32) Fan, X.; et al. Non-flammable electrolyte enables Li-metal batteries with aggressive cathode chemistries. *Nat. Nanotechnol.* **2018**, *13*, 715–722.
- (33) Fan, X.; et al. All-temperature batteries enabled by fluorinated electrolytes with non-polar solvents. *Nat. Energy* **2019**, *4*, 882–890.
- (34) Xue, W.; et al. FSI-inspired solvent and “full fluorosulfonyl” electrolyte for 4 V class lithium-metal batteries. *Energy Environ. Sci.* **2020**, *13*, 212–220.
- (35) Rustomji, C. S.; et al. Liquefied gas electrolytes for electrochemical energy storage devices. *Science* **2017**, *356*, No. eaal4263.
- (36) Yang, Y.; et al. High-Efficiency Lithium-Metal Anode Enabled by Liquefied Gas Electrolytes. *Joule* **2019**, *3*, 1986–2000.
- (37) Yang, Y.; et al. Liquefied gas electrolytes for wide-temperature lithium metal batteries. *Energy Environ. Sci.* **2020**, *13*, 2209–2219.
- (38) Yu, Z.; et al. Molecular design for electrolyte solvents enabling energy-dense and long-cycling lithium metal batteries. *Nat. Energy* **2020**, *5*, 526–533.
- (39) Li, Y.; et al. Atomic structure of sensitive battery materials and interfaces revealed by cryo-electron microscopy. *Science* **2017**, *358*, 506.
- (40) Peled, E. The Electrochemical Behavior of Alkali and Alkaline Earth Metals in Nonaqueous Battery Systems—The Solid Electrolyte Interphase Model. *J. Electrochem. Soc.* **1979**, *126*, 2047.
- (41) Peled, E.; Golodnitsky, D.; Ardel, G. Advanced Model for Solid Electrolyte Interphase Electrodes in Liquid and Polymer Electrolytes. *J. Electrochem. Soc.* **1997**, *144*, L208.
- (42) Aurbach, D. Identification of Surface Films Formed on Lithium in Propylene Carbonate Solutions. *J. Electrochem. Soc.* **1989**, *136*, 1611.
- (43) Li, Y.; et al. Correlating Structure and Function of Battery Interphases at Atomic Resolution Using Cryoelectron Microscopy. *Joule* **2018**, *2*, 2167–2177.
- (44) Genovese, M.; et al. Hot Formation for Improved Low Temperature Cycling of Anode-Free Lithium Metal Batteries. *J. Electrochem. Soc.* **2019**, *166*, A3342–A3347.
- (45) Louli, A. J.; et al. Exploring the Impact of Mechanical Pressure on the Performance of Anode-Free Lithium Metal Cells. *J. Electrochem. Soc.* **2019**, *166*, A1291–A1299.
- (46) Zhang, X.; et al. Rethinking How External Pressure Can Suppress Dendrites in Lithium Metal Batteries. *J. Electrochem. Soc.* **2019**, *166*, A3639–A3652.
- (47) Fang, C.; et al. Quantifying inactive lithium in lithium metal batteries. *Nature* **2019**, *572*, 511–515.
- (48) Heiskanen, S. K.; Kim, J.; Lucht, B. L. Generation and Evolution of the Solid Electrolyte Interphase of Lithium-Ion Batteries. *Joule* **2019**, *3*, 2322–2333.
- (49) Shin, H.; Park, J.; Han, S.; Sastry, A. M.; Lu, W. Component-/structure-dependent elasticity of solid electrolyte interphase layer in Li-ion batteries: Experimental and computational studies. *J. Power Sources* **2015**, *277*, 169–179.

(50) Weadock, N.; et al. Determination of mechanical properties of the SEI in sodium ion batteries via colloidal probe microscopy. *Nano Energy* **2013**, *2*, 713–719.

(51) Yoon, I.; Jung, S.; Abraham, D. P.; Lucht, B. L.; Guduru, P. R. In Situ Measurement of the Plane-Strain Modulus of the Solid Electrolyte Interphase on Lithium-Metal Anodes in Ionic Liquid Electrolytes. *Nano Lett.* **2018**, *18*, 5752–5759.

(52) Liu, S.; et al. High Interfacial-Energy Interphase Promoting Safe Lithium Metal Batteries. *J. Am. Chem. Soc.* **2020**, *142*, 2438–2447.

(53) Pathak, R.; et al. Fluorinated hybrid solid-electrolyte-interphase for dendrite-free lithium deposition. *Nat. Commun.* **2020**, *11*, 93.

(54) Zheng, G.; et al. High-Performance Lithium Metal Negative Electrode with a Soft and Flowable Polymer Coating. *ACS Energy Lett.* **2016**, *1*, 1247–1255.

(55) Lu, Y.; Tu, Z.; Archer, L. A. Stable lithium electrodeposition in liquid and nanoporous solid electrolytes. *Nat. Mater.* **2014**, *13*, 961–969.

(56) Xie, J.; et al. Stitching h-BN by atomic layer deposition of LiF as a stable interface for lithium metal anode. *Sci. Adv.* **2017**, *3*, No. eaao3170.

(57) Lin, D.; et al. Conformal Lithium Fluoride Protection Layer on Three-Dimensional Lithium by Nonhazardous Gaseous Reagent Freon. *Nano Lett.* **2017**, *17*, 3731–3737.

(58) Wang, X.; et al. New Insights on the Structure of Electrochemically Deposited Lithium Metal and Its Solid Electrolyte Interphases via Cryogenic TEM. *Nano Lett.* **2017**, *17*, 7606–7612.

(59) Huang, W.; Wang, H.; Boyle, D. T.; Li, Y.; Cui, Y. Resolving Nanoscopic and Mesoscopic Heterogeneity of Fluorinated Species in Battery Solid-Electrolyte Interphases by Cryogenic Electron Microscopy. *ACS Energy Lett.* **2020**, *5*, 1128–1135.